NANO LETTERS

ACS AUTHORCHOICE

pubs.acs.org/NanoLett

Letter

# Heat Driven Transport in Serial Double Quantum Dot Devices

Sven Dorsch,* Artis Svilans, Martin Josefsson, Bahareh Goldozian, Mukesh Kumar, Claes Thelander, Andreas Wacker,* and Adam Burke*

Cite This: *Nano Lett.* 2021, 21, 988−994

Read Online

ACCESS | Metrics & More | Article Recommendations | Supporting Information

**ABSTRACT:** Studies of thermally induced transport in nanostructures provide access to an exciting regime where fluctuations are relevant, enabling the investigation of fundamental thermodynamic concepts and the realization of thermal energy harvesters. We study a serial double quantum dot formed in an InAs/InP nanowire coupled to two electron reservoirs. By means of a specially designed local metallic joule-heater, the temperature of the phonon bath in the vicinity of the double quantum dot can be enhanced. This results in phonon-assisted transport, enabling the conversion of local heat into electrical power in a nanosized heat engine. Simultaneously, the electron temperatures of the reservoirs are affected, resulting in conventional thermoelectric transport. By detailed modeling and experimentally tuning the interdot coupling, we disentangle both effects. Furthermore, we show that phonon-assisted transport is sensitive to excited states. Our findings demonstrate the versatility of our design to study fluctuations and fundamental nanothermodynamics.

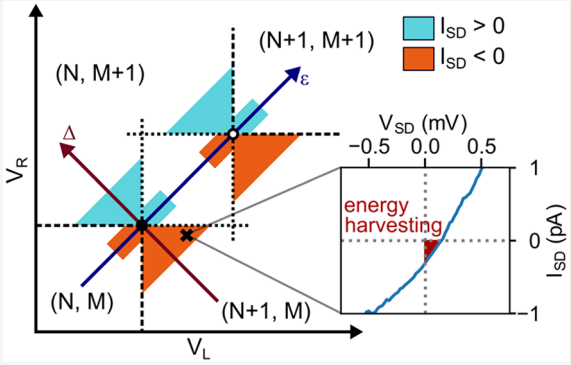


**KEYWORDS:** *nanowire, thermoelectric effect, phonon assisted transport, quantum dot, thermal energy harvesters*

Serial double quantum dot (DQD) devices are attractive systems for both fundamental quantum physics studies and quantum electronic-based applications with well-established charge transport properties.[1−3] Because of the electronic structure[4] and controllable level detunement, DQDs are highly sensitive to their environment. Consequently, interactions of DQDs with their charge environment, photons,[5,6] and phonons[7−17] have been demonstrated and used for frequency resolved noise, photon, and phonon detection.[18−20]

In this Letter, we study the impact of interactions between a DQD and its thermal environment on transport across the device. The relation between electrical transport and temperature gradients in nanoscale systems is important for applications as energy harvesters[21−28] or fundamental studies of statistical physics.[29−33] In a conventional setup, thermoelectricity is driven by the temperature difference created between electrical probes of a circuit which induces a current. Here, in addition to the thermoelectric effect (TE) across a DQD, we consider how a thermal reservoir decoupled from the electronic circuit of the device affects currents by phonon-assisted transport (PAT). We demonstrate how PAT and the TE can be unambiguously distinguished and used to probe excited states. Furthermore, we show experimentally that PAT can be used to harvest energy from the heated lattice in a three-terminal geometry, which is a concept proposed by Entin-Wohlman et al.[34] and theoretically studied for a variety of related systems.[35−39]

Our experimental device is shown in Figure 1a. A DQD is epitaxially formed within an InAs nanowire via three InP segments.[40,41] Plunger gates control the energy levels of the left and right quantum dot (QD) by applying a voltage $V_{L(R)}$ to the left (right) plunger gate. The DQD device is coupled to the thermal reservoirs in the contacts with electron temperatures $T_S$ and $T_D$ of the source and drain contact, respectively. Additionally, the lattice acts as third thermal reservoir with a phonon temperature $T_{ph}$. A metallic joule-heater electrode in close vicinity to the nanowire, decoupled from the electronic system of the DQD, serves as an external heat source. By design, a current driven through the joule-heater by a heating bias $dV_H = |V_{H1} - V_{H2}|$ heats the lattice more than the electron reservoirs of the DQD. A small misalignment of the electrode with the DQD structure in the nanowire further leads to an asymmetric impact on the contact electron temperatures.

In the following, we describe the device as a DQD with small interdot tunnel coupling Ω, that is weakly coupled to the source and drain electron reservoirs. Figure 1b illustrates the charge stability diagram of the DQD in plunger gate space

**Received:** October 7, 2020
**Revised:** January 12, 2021
**Published:** January 18, 2021

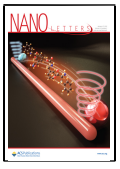

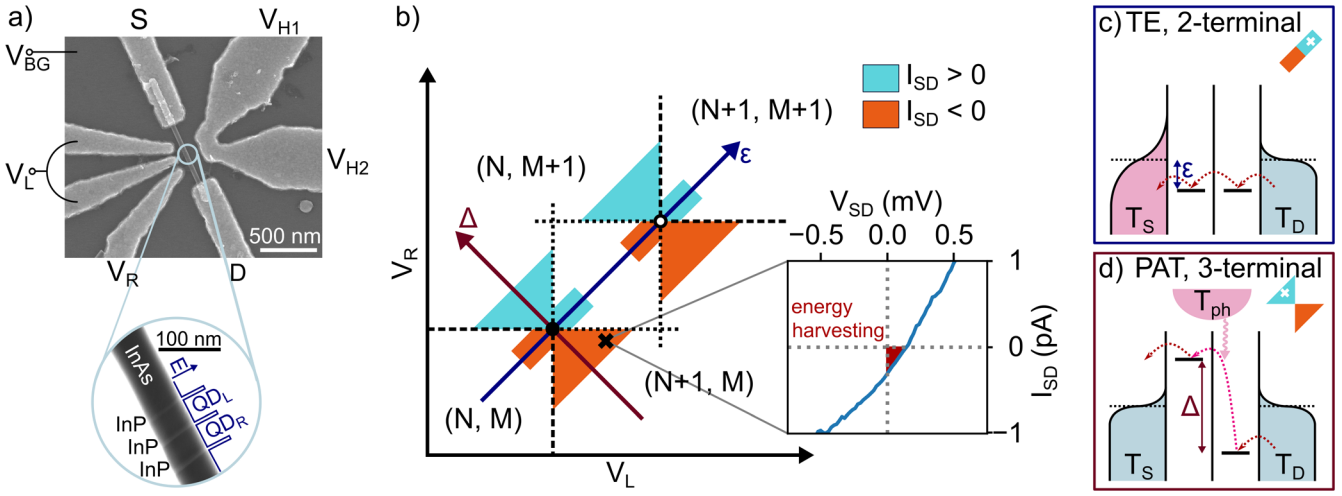


**Figure 1.** (a) Scanning electron microscope image of the device. An InAs/InP nanowire on a substrate acting as backgate ($V_{BG}$) is contacted ($S$, $D$) and plunger gates ($V_L$, $V_R$) are placed in close vicinity to the DQD. The inset shows a transmission mode scanning electron microscope image of the nanowire. Three InP segments embedded in the InAs nanowire serve as tunnel barriers to epitaxially form a DQD. A heater electrode ($V_{H1}$, $V_{H2}$) is aligned with the DQD to heat the device. (b) Schematic illustration of temperature gradient driven currents in the charge stability diagram of DQD devices in the absence of external bias. Colored regions illustrate where currents are induced by the TE or PAT for the case $T_{ph} > T_S > T_D$ around the $(N, M) \rightarrow (N + 1, M + 1)$ transition. Inset: Experimental six-time averaged $I_{SD}$−$V_{SD}$ curve, measured with a heating bias of $dV_H = 4$ V at a point corresponding to the black cross in the charge stability diagram. The offset of the curve toward the origin indicates that the device produces power. (c) Schematic illustration of the TE, inducing transport along the energy axis $\epsilon = \mu - (E_L + E_R)/2$. (d) Schematic illustration of PAT along the level detunement axis $\Delta = E_L - E_R$. The insets in (c,d) show the characteristic current patterns around the TP and the white crosses indicate the location of the level combinations shown in the panel.

around a pair of triple points (TP) in the $(N, M) \rightarrow (N + 1, M + 1)$ charge transition region. The black and white dots label the position of electron and hole TPs, respectively. Here, we assume that due to substantial charging and level-quantization energies only a single level with energy $E_L/E_R$ can be additionally occupied in the left/right dot containing already $N/M$ electrons in this region. These addition energies are essentially linear functions of the gate voltages $E_{L/R} = \alpha_{L/R}(V^T_{L/R} - V_{L/R})$, where $V^T_{L/R}$ are the voltages at the electron triple point and $\alpha_{L/R}$ are the lever arm factors. For the sake of convenience, we define local coordinates $\epsilon = \mu - (E_L + E_R)/2$ and $\Delta = E_L - E_R$, where $\mu = \mu_S = \mu_D$ is the chemical potential for vanishing source-drain bias $V_{SD} = 0$ V. Charging lines separate regions of different overall charge (dashed lines) and upon crossing the charge transfer line, connecting the two TPs along $\epsilon$, an electron is transferred from one QD to the other. In the absence of photons, phonons, or a driving bias voltage, no net current flows and conductivity is only expected on the TPs. Cyan (orange) shaded areas indicate where heating the device via the joule-heater electrode can drive positive (negative) currents in the absence of a voltage bias.

The TE illustrated in Figure 1c occurs when $T_S \neq T_D$. The effect manifests along the axis $\epsilon$ when levels in each QD are aligned and moved in energy together. The applied temperature gradient causes different energy distributions of the electronic reservoirs around the electrochemical potentials $\mu$. The DQD connecting the two reservoirs acts as an energy filter probing the electron population imbalance at a set energy.[42] For $\epsilon < 0$ ($\epsilon > 0$), this causes electrons to flow from hot to cold (cold to hot). Consequently a reversal of the thermoelectric current polarity is observed upon crossing each TP along $\epsilon$. This effect has been studied in single QD devices[26,42−47] as well as in DQDs.[48]

PAT via phonon absorption is an inelastic transport mechanism requiring a detuned two-level system. Along the energy axis, $\Delta = E_L - E_R$ levels on the two QDs are energetically detuned, as illustrated for $\Delta > 0$ in Figure 1d. For large $\Delta$, thermoelectric currents are blocked. Electrons can then only be transported from the energetically lower occupied to the higher unoccupied energy level of the DQD by absorbing a phonon from the hot phonon bath, and a net current can flow if $T_{ph} > T_S$, $T_D$.[49] Reverting the sign of $\Delta$ (crossing the charge transfer line where $\Delta = 0$) causes the electron transport to revert direction. Consequently, PAT yields currents of opposite polarity on opposite sides of the charge transfer line as long as the spectral distribution of the phonon bath provides sufficient phonon energies to overcome the DQD level detuning. For $|\Delta| \gg k_B T_{ph}$, this condition is no longer fulfilled and PAT is suppressed. We note that a significant difference in occupation between the initial and final state for the PAT process is required.[49] Without external bias, this requirement is only fulfilled if the two involved states are on opposite sides of the Fermi surface. Thus, PAT active regions are limited to triangular areas within the charge stability diagram as shown in Figure 1b.[3,8]

Within these active regions, it is possible to harvest energy from an external heat source, as demonstrated in the inset of Figure 1b. Successful operation of our device as a three-terminal energy harvester at $dV_H = 4$ V is evident by the nonzero current $I_{SD}$ at $V_{SD} = 0$ V. Considering $R \approx 1$ MΩ in series with the device, as used for this measurement, we extract a power of $P = RI^2_{SD} \approx 0.1$aW.[26,50] In the limit of weak tunnel couplings, this translates to an upper bound for the unoptimized efficiency of the electronic system, $\eta = P/Q_H = (RI_{SD}e)/\Delta = 0.03\%$.[24] Here, the heat flow $Q_H = \Delta I_{SD}/e$ describes the energy gain of the detected electrons upon phonon absorption.

To experimentally study heat driven currents in our device, we first characterize the DQD via conventional finite bias spectroscopy and pick a range in the intermediate (Figure 2a)


https://dx.doi.org/10.1021/acs.nanolett.0c04017
Nano Lett. 2021, 21, 988−994

and weak (Figure 2b) interdot coupling regime. Details of the device characterization and measurement conditions are given in the Supporting Information (SI).

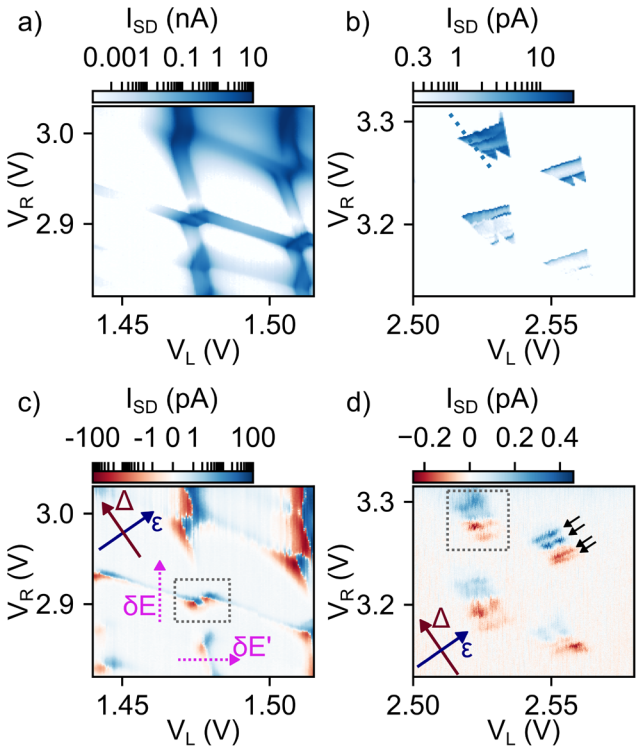


**Figure 2.** (a) Bias driven current $I_{SD}$ as a function of the plunger gate voltages $V_L$ and $V_R$ at $V_{H1} = V_{H2} = -4$ V, $V_{BG} = 0$ V and $V_{SD} = 1$ mV in the intermediate interdot coupling regime. (b) Bias driven current $I_{SD}$ in the weak interdot coupling regime with$V_{H1} = V_{H2} = -4$ V, $V_{BG} = -1$ V and $V_{SD} = 3$ mV. (c) Experimental heat driven current $I_{SD}$ as a function of the plunger gate voltages measured at $V_{SD} = 0$ V and $dV_H = 1$ V in the intermediate interdot coupling regime. The current is plotted on a logarithmic scale with a linear range between ±1 pA. (d) Experimental heat driven current $I_{SD}$, measured at $V_{SD} = 0$ V and $dV_H = 4$ V in the weak interdot coupling regime. Dotted, gray rectangles in (c,d) label a comparable small range around a single set of TPs as in Figure 1b.

We now demonstrate a key capability of this study: By controlling the interdot tunnel coupling, we tune the dominant mechanism behind thermally driven currents between the TE and PAT. Figure 2c,d presents exemplary measurements of purely thermally driven currents $I_{SD}$ across a heated DQD as a function of the plunger gate voltages $V_L$ and $V_R$ in the intermediate (c) and weak (d) interdot coupling regimes. These measurements effectively map heat driven transport signals within the DQD charge stability diagram. While maintaining $T_{ph} > T_S > T_D$ in both measurements, we experimentally find apparent differences in heat driven transport in the intermediate and weak interdot coupling regimes. A detailed characterization of the signals at different heating bias $dV_H$ is given in the SI.

In the intermediate interdot coupling regime (Figure 2c), the pronounced polarity reversal of current close to the TPs occurs along the energy axis $\epsilon$, suggesting the thermoelectric effect to be the main transport mechanism. Further, signals also appear along the charging lines and are in good agreement with thermoelectric transport across an intermediately coupled DQD observed by Thierschmann et al.[48] In contrast, in the weak interdot coupling regime (Figure 2d) currents reverse the sign perpendicular to $\epsilon$, along $\Delta$, which is characteristic for a PAT dominated system. With the exception of pronounced resonances (black arrows), our results qualitatively match previous studies on phonon-mediated back action of charge sensors on transport through weakly coupled DQDs.[8,11,12,15]

To explain the difference between the intermediate and weak interdot coupling regime, we consider the impact of the interdot tunnel coupling $\Omega$ on heat driven transport. Discrete energy levels $E_L$ and $E_R$ confined to the left and right QD respectively only exist for $\Delta \gg \Omega$ when mixing effects are suppressed.[18] In contrast, if $\Delta \gg \Omega$ is not fulfilled, the electronic wave functions will extend over both QDs, and mixing of $E_L$ and $E_R$ leads to the formation of bonding and antibonding molecular states $E_{bond}$, $E_{antibond}$.[51] The molecular states are energetically separated by

$$E_{antibond} - E_{bond} = [(E_L - E_R)^2 + 4\Omega^2]^{1/2} \quad (1)$$

and have direct consequences on both PAT and the thermoelectric effect.[52]

For PAT, the formation of bonding and antibonding molecular states introduces new, additional constraints as phonons now have to supply a minimum energy of $E_{ph} > 2\Omega$ even at small $\Delta$, which agrees with observations in photon-assisted transport experiments.[52] Consequently, the onset of PAT is offset toward higher phonon energies and temperatures with increasing $\Omega$. In addition, as a result of the electronic wave functions extending across both QDs[51] the directionality of PAT is reduced as electrons now have an increased probability to tunnel back into their initial reservoir and not contribute to the detected PAT current signal. The thermoelectric effect on the other hand benefits from the formation of molecular states. Although for $\Delta \gg \Omega$, elastic thermoelectric transport is blocked, for large $\Omega$ this blockade is lifted due to the extended wave functions, and thermoelectric current contributions can be observed in an increased range along $\Delta$. Finally, along the more horizontal (vertical) charging lines where a level in the right (left) QD is aligned with $\mu_{SD}$, the DQD behaves as single QD with an effective left (right) tunnel coupling $\Gamma_{L(R),eff} \approx \Gamma_{L(R)}\Omega^2/\Delta^2$.[53] As a result of the high $\Omega$, currents are observed along these charging lines in the heated case which along an energy axis $\delta E$ ($\delta E'$) resembles a pure TE across a single QD because no final state for a PAT process is available.

We use the observation of pure TE signals along the charging lines in the intermediate interdot coupling regime to estimate contact electron temperatures $T_{S/D}$ independently of the phonon temperature and find

$$T_S \approx 0.90\ \text{K/V}\cdot dV_H + 0.13\ \text{K}$$
$$T_D \approx 0.87\ \text{K/V}\cdot dV_H + 0.13\ \text{K} \quad (2)$$

Here, the small temperature difference is in good agreement with our expectations for a nearly symmetric heating effect of the heater electrode. Details of the contact electron temperature estimation are given in the SI.

In order to disentangle the individual TE and PAT contributions to the experimental signal further, we performed detailed simulations of the transport through a DQD system with two spin degenerate levels in each QD (ground levels $E_{L/R}$ and excited levels with spacing $\Delta E_L = 0.8$ meV and $\Delta E_R = 1.7$ meV). Furthermore, we use the Coulomb interaction terms for intradot $U = 8$ meV, for interdot $U_n = 1.4$ meV, and for


https://dx.doi.org/10.1021/acs.nanolett.0c04017
Nano Lett. 2021, 21, 988−994

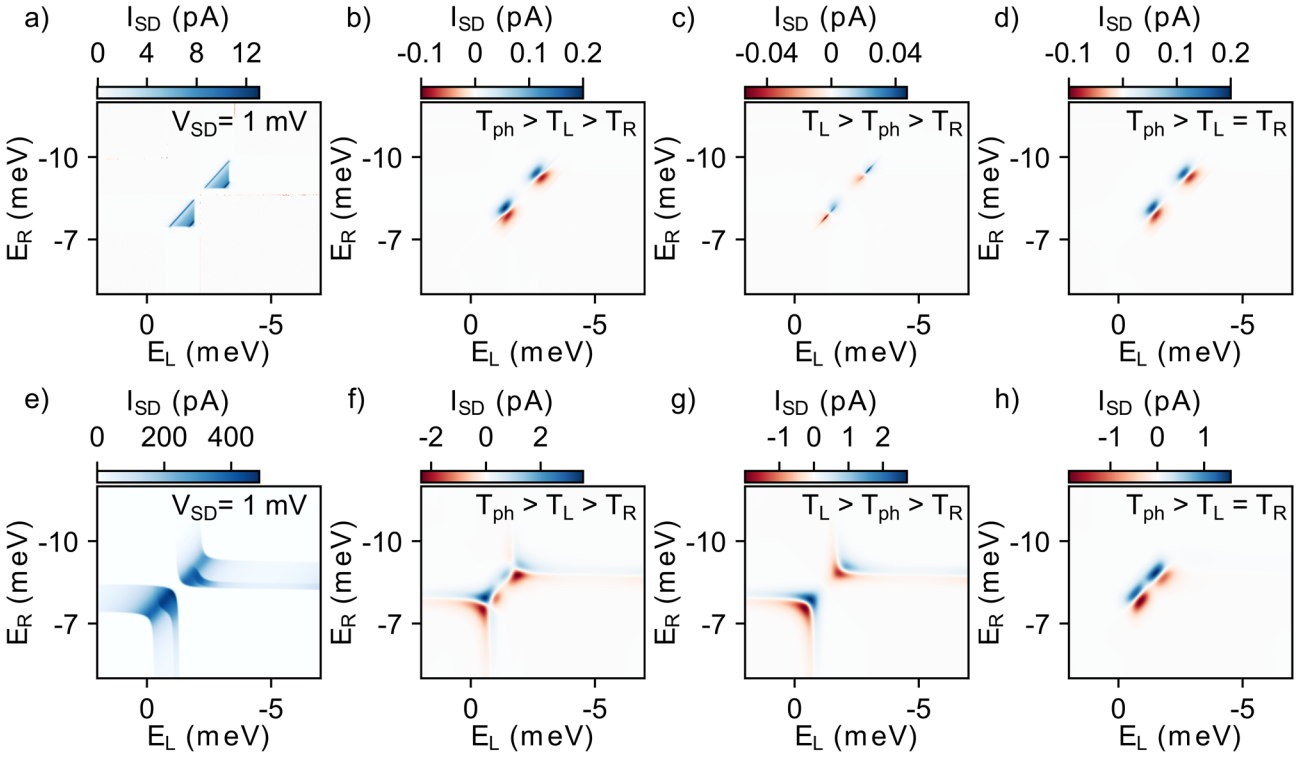


**Figure 3.** Simulated charge stability diagram around the (0,1) → (1,2) charge state transition in the weak (a−d) and intermediate (e−h) interdot coupling regime. (a,e) Finite bias spectroscopy at $V_{SD}$ = 1 mV, $dV_H$ = 0 V and $T_S = T_D = T_{ph}$ = 130 mK. Heat driven currents are simulated at $V_{SD}$ = 0 mV and $dV_H$ = 1 V in the weak (b−d) and intermediate (f−h) interdot coupling regime. (b,f) Temperatures $T_{ph}$, $T_S$, and $T_D$ are set using eqs 2 and 3. In (c,g) $T_{ph}$ is replaced by the average of $T_S$ and $T_D$, whereas in (d,h) we use $T_S = T_D$ = 0.9 K/V·$dV_H$ + 130 mK and $T_{ph}$ is set by eq 3.

intradot exchange $U_{ex}$ = 0.4 meV. These parameters are motivated in the SI, where additional simulation details are given. All transport simulations are done with the open source simulation tool QMEQ [Quantum Master Equation for Quantum dot transport calculations][54] with the recent inclusion of phonon scattering.[49] To model the side-heating, we assume the phonon temperature

$$T_{ph} = 1.2\ \text{K/V}\cdot dV_H + 0.13\ \text{K} \tag{3}$$

as the heating bias $dV_H$ should have a stronger impact on the phonons in the DQD than on the electrons in the leads, compare eq 2 which is simultaneously used here. Here, we focus on the (0, 1) → (1, 2) charge transition region, which appears to give best agreement with the experimental data.

Figure 3a,e shows simulation results for a fixed $V_{SD}$ = 1 mV without heating. For the weak interdot coupling case (upper panels), the current shows distinct triangles around the triple points. Instead, for the simulated intermediate interdot coupling case (lower panels), anticrossing behavior is visible and is qualitatively in agreement with the experimental data in Figure 2a. With heating, the panels (b,f) correspond to, and qualitatively agree with the gray rectangles in Figure 2c,d and show the typical pure heat driven current distribution due to combined PAT and TE currents for $T_{ph} > T_S > T_D$. In the simulations, we are able to disentangle both effects by separate modification of the temperatures. In panels (c,g), the PAT contribution is removed by setting the phonon temperature as the mean of temperatures in the source and drain contact. Here, we obtain a current profile, where the sign changes only along the axis $\epsilon$ in vicinity to the TPs. In the intermediate interdot coupling regime, signals further extend along the charging lines. In contrast, if we remove the TE contribution by assuming $T_{ph} > T_S = T_D$, see Figure 3d,h, the pure PAT current reverses polarity along the Δ axis near the TPs exclusively.

In the weak coupling regime, thermoelectric currents are an order of magnitude smaller than PAT currents (compare Figure 3c,d). This is a result of the PAT driving temperature difference $T_{ph} - T_S$ growing faster with $dV_H$ compared to the difference $T_S - T_D$ driving the TE. Consequently, the mixed signal in Figure 3b appears almost exclusively PAT-like. In contrast, in the intermediate coupling regime PAT is suppressed and the TE benefits from the increased interdot coupling. The TE and PAT contributions here, see Figure 3g,h, are of comparable magnitude for the chosen $dV_H$ = 1 V and the mixed signal in panel (f) shows a complex superposition as observed in the experiment.

Finally, we return to weak interdot coupling and address the pronounced resonances within Figure 2d (black arrows), which were not observed by previous PAT or thermoelectric effect related studies. Comparable features are reported for experiments based on photon-assisted transport across DQDs and are attributed to multiphoton processes.[5,52] In contrast to those experiments, we find the resonances in Figure 2d (and SI) to be asymmetric with respect to the charge transfer line. This asymmetry, in combination with the continuous PAT signal along Δ, rules out resonant one- and two-phonon processes. To study the origin of the resonances, we combine finite bias spectroscopy with heated measurements.

Figure 4a shows the current $I_{SD}$ without heating, $dV_H$ = 0 V, as a function of $V_{SD}$ along the cut-line Δ, marked by a blue dotted line in Figure 2b. The cut-line is chosen such that it crosses finite bias triangles forming in both positive and negative $V_{SD}$ direction. We note that the observed linear slope


https://dx.doi.org/10.1021/acs.nanolett.0c04017
Nano Lett. 2021, 21, 988−994

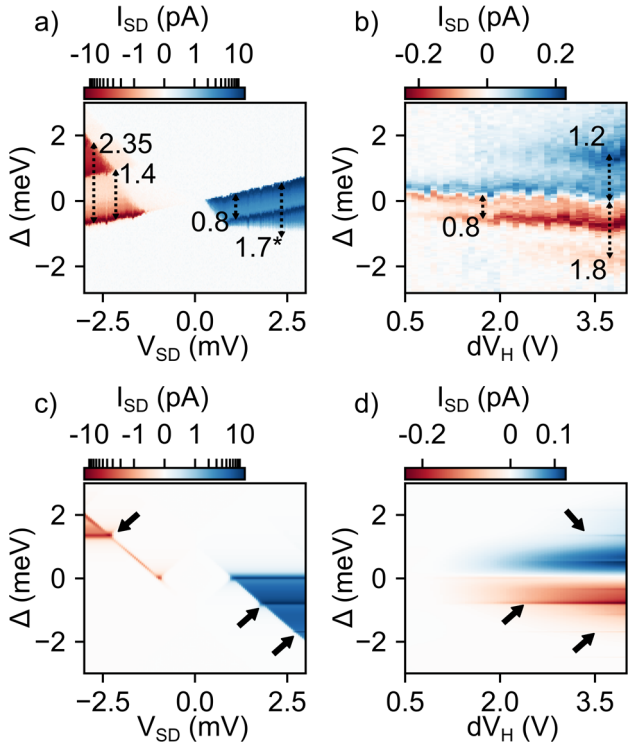


**Figure 4.** (a) Current measurement along the cut-line Δ (blue dotted line in Figure 2b) as a function of the driving bias $V_{SD}$ at $dV_H$ = 0 V. The current is plotted on a logarithmic scale with a linear range between ±1 pA. (b) Current along Δ as a function of the heater voltage bias $dV_H$ at $V_{SD}$ = 0 V. Numbers in (a) and (b) correspond to the energetic spacing from resonance to the charge transfer line in millielectronvolts, indicated by dotted black arrows. The excited state at 1.7 meV (labeled by * in (a)) is slightly outside the overlap of the cut-line with the bias triangle and the spacing is read out from Figure 2b. Each data point in (a) and (b) is the result of two-time averaging. (c) Simulation of (a) at $T_{ph} = T_S = T_D$ = 130 mK. (d) Simulation of (b) using the temperature calibrations given in eqs 2 and 3. Black arrows in (c,d) label energetically matching resonances within the bias and heat driven simulated currents.

of the groundstate (GS) to groundstate transition line (the charge transfer line), where the energetically lowest available state in each QD mediates transport, is an effect of the source contact's capacitive coupling to the DQD. Δ is manually set to zero where the charge transfer line intersects with $V_{SD}$ = 0 V. For positive (negative) $V_{SD}$ we detected how the finite bias triangle grows in height with negative (positive) Δ. Sudden changes in current are observed when a new excited state (ES) becomes available for transport and is initially aligned with the GS in the other QD. This allows mapping of the GS−ES spacing for the left (Δ < 0) and right (Δ > 0) QD. The values for the GS−ES spacings in millielectronvolts are annotated in Figure 4a. For positive $V_{SD}$, an additional GS−ES spacing of 1.7 meV (labeled by *) is obtained from Figure 2b. We note that the current suppression before the triplet state becomes available (below 1.4 meV) within the finite bias triangle for negative $V_{SD}$ is Pauli spin blockaded.[55−57] The spin blockade is lifted along the GS−GS transition, possibly due to hyperfine- or spin−orbit-interaction.[58] Further, the change in slope of the triangle outline for $V_{SD}$ > 0 and Δ < −0.8 meV is a result of the chosen cut-line position which ceases to overlap with the triangle.

Figure 4b shows the current $I_{SD}$ along the cut-line Δ as a function of $dV_H$ for $V_{SD}$ = 0 V. The PAT-induced current polarity reversal at Δ = 0 is clearly visible. With increasing $dV_H$, the phonon temperature $T_{ph}$ increases, which provides larger currents. Furthermore, the PAT currents are visible for |Δ| being less than a few $k_B T_{ph}$, as phonons with higher energies are entirely frozen out. Thus, the PAT active regions grow with increasing $dV_H$. Resonances, as observed in Figure 2d, begin to appear with increasing heating voltages $dV_H$. The energy spacing in millielectronvolts from resonance to charge transfer line is annotated in Figure 4b, and we find similar values to the GS−ES spacings in Figure 4a.

One possible cause for the resonances is a TE through aligned GS−ES configurations. This would lead to a polarity reversal of the current on the resonances once the aligned GS−ES levels are energetically pulled below $\mu$ as we follow the resonance in direction of $\epsilon$. We interpret the absence of this polarity reversal in Figure 2d as an indication of PAT through excited states as origin for the resonances.

To confirm a PAT process as the origin of the resonances, we simulate the bias and purely heat driven currents along a cut-line $\Delta = E_L - E_R - \Delta_0$ in Figure 4c,d, corresponding to the experiments in Figure 4a,b. Here, for $E_L = E_R + \Delta_0$ the ground states GS(1, 1) and GS(0, 2) are in resonance. For biased transport, in Figure 4c spin blockade is observed until the triplet ES(0, $2_e$) gets in resonance with GS(1, 1) for negative $V_{SD}$ but in contrast to the experiment no partial lifting by hyperfine- or spin−orbit interaction is considered.

By comparison of Figure 4c,d to their experimental counterparts, we first find good qualitative agreement. Second, we identify matching resonances in Figure 4c,d, labeled by black arrows and identify the relevant transport mechanism in the simulations as PAT through excited states. A detailed identification of the different transitions responsible for the current peaks is given in the SI.

In summary, we present a detailed, combined experimental and theoretical study of heat driven transport in a DQD coupled to three thermal reservoirs. We show how via tuning the interdot tunnel coupling, the dominant transport mechanism can be tuned between the two-terminal TE and three-terminal PAT, which is further found to be sensitive to excited states. Consequently, we demonstrate the applicability of conventional DQD devices as highly versatile and controllable energy harvesters and provide a platform and the tools to conduct and analyze fundamental nanothermodynamic experiments.

General conclusions about the performance and ideal operating conditions of our device as an energy harvester are complex to draw due to the high degree of freedom and require knowledge of the phonon spectral function to accurately determine $T_{ph}$. Conceptually similar systems have in that regard been only theoretically analyzed.[38,59] We thus consider future experiments combining access to the phonon spectral function[17] with a dedicated study of the energy harvesting performance of our system as highly interesting.

## ■ ASSOCIATED CONTENT

### Supporting Information

The Supporting Information is available free of charge at https://pubs.acs.org/doi/10.1021/acs.nanolett.0c04017.

Device fabrication and measurement details including finite bias spectroscopy, bias offset characterization,



https://dx.doi.org/10.1021/acs.nanolett.0c04017
Nano Lett. 2021, 21, 988−994

contact electron temperature estimations, detailed characterization of the heat driven current signal in the weak and intermediate interdot coupling regime as well as simulation details, analysis of tunnelling via excited states, and further simulations (PDF)

## AUTHOR INFORMATION


### Corresponding Authors

**Sven Dorsch** − *Solid State Physics and NanoLund, Lund University, SE-221 00 Lund, Sweden;* orcid.org/0000-0002-4314-945X; Email: sven.dorsch@ftf.lth.se

**Andreas Wacker** − *Mathematical Physics and NanoLund, Lund University, SE-221 00 Lund, Sweden;* Email: andreas.wacker@fysik.lu.se

**Adam Burke** − *Solid State Physics and NanoLund, Lund University, SE-221 00 Lund, Sweden;* orcid.org/0000-0001-9345-2812; Email: adam.burke@ftf.lth.se

### Authors

**Artis Svilans** − *Solid State Physics and NanoLund, Lund University, SE-221 00 Lund, Sweden*

**Martin Josefsson** − *Solid State Physics and NanoLund, Lund University, SE-221 00 Lund, Sweden*

**Bahareh Goldozian** − *Mathematical Physics and NanoLund, Lund University, SE-221 00 Lund, Sweden*

**Mukesh Kumar** − *Solid State Physics and NanoLund, Lund University, SE-221 00 Lund, Sweden*

**Claes Thelander** − *Solid State Physics and NanoLund, Lund University, SE-221 00 Lund, Sweden*

Complete contact information is available at: https://pubs.acs.org/10.1021/acs.nanolett.0c04017


### Notes

The authors declare no competing financial interest.

## ACKNOWLEDGMENTS

The authors thank H. Linke for fruitful discussions and acknowledge funding by the Knut and Alice Wallenberg Foundation (KAW) (Project 2016.0089), the Swedish Research Council (VR) (Project 2015-00619), the Marie Skłodowska Curie Actions, Cofund, Project INCA 600398 and by NanoLund. Device fabrication was carried out in the Lund Nano Lab (LNL), and computational resources were provided by the Swedish National Infrastructure for Computing (SNIC) at LUNARC.

## REFERENCES


(1) Bennett, C. H.; DiVincenzo, D. P. Quantum information and computation. *Nature* **2000**, *404*, 247−255.

(2) Hanson, R.; Kouwenhoven, L. P.; Petta, J. R.; Tarucha, S.; Vandersypen, L. M. K. Spins in few-electron quantum dots. *Rev. Mod. Phys.* **2007**, *79*, 1217−1265.

(3) van der Wiel, W. G.; De Franceschi, S.; Elzerman, J. M.; Fujisawa, T.; Tarucha, S.; Kouwenhoven, L. P. Electron transport through double quantum dots. *Rev. Mod. Phys.* **2002**, *75*, 1−22.

(4) Reimann, S. M.; Manninen, M. Electronic structure of quantum dots. *Rev. Mod. Phys.* **2002**, *74*, 1283−1342.

(5) Petta, J. R.; Johnson, A. C.; Marcus, C. M.; Hanson, M. P.; Gossard, A. C. Manipulation of a Single Charge in a Double Quantum Dot. *Phys. Rev. Lett.* **2004**, *93*, 186802.

(6) Qin, H.; Holleitner, A. W.; Eberl, K.; Blick, R. H. Coherent superposition of photon- and phonon-assisted tunneling in coupled quantum dots. *Phys. Rev. B: Condens. Matter Mater. Phys.* **2001**, *64*, 241302.

(7) Fujisawa, T.; Oosterkamp, T. H.; van der Wiel, W. G.; Broer, B. W.; Aguado, R.; Tarucha, S.; Kouwenhoven, L. P. Spontaneous Emission Spectrum in Double Quantum Dot Devices. *Science* **1998**, *282*, 932−935.

(8) Granger, G.; Taubert, D.; Young, C. E.; Gaudreau, L.; Kam, A.; Studenikin, S. A.; Zawadzki, P.; Harbusch, D.; Schuh, D.; Wegscheider, W.; Wasilewski, Z. R.; Clerk, A. A.; Ludwig, S.; Sachrajda, A. S. Quantum interference and phonon-mediated back-action in lateral quantum-dot circuits. *Nat. Phys.* **2012**, *8*, 522−527.

(9) Gasser, U.; Gustavsson, S.; Küng, B.; Ensslin, K.; Ihn, T.; Driscoll, D. C.; Gossard, A. C. Statistical electron excitation in a double quantum dot induced by two independent quantum point contacts. *Phys. Rev. B: Condens. Matter Mater. Phys.* **2009**, *79*, 035303.

(10) Naber, W. J. M.; Fujisawa, T.; Liu, H. W.; van der Wiel, W. G. Surface-Acoustic-Wave-Induced Transport in a Double Quantum Dot. *Phys. Rev. Lett.* **2006**, *96*, 136807.

(11) Khrapai, V. S.; Ludwig, S.; Kotthaus, J. P.; Tranitz, H. P.; Wegscheider, W. Nonequilibrium interactions between two quantum circuits. *J. Phys.: Condens. Matter* **2008**, *20*, 454205.

(12) Khrapai, V.; Ludwig, S.; Kotthaus, J.; Tranitz, H.; Wegscheider, W. Nonequilibrium phenomena in adjacent electrically isolated nanostructures. *Phys. E* **2008**, *40*, 995−998.

(13) Weber, C.; Fuhrer, A.; Fasth, C.; Lindwall, G.; Samuelson, L.; Wacker, A. Probing Confined Phonon Modes by Transport through a Nanowire Double Quantum Dot. *Phys. Rev. Lett.* **2010**, *104*, 036801.

(14) Roulleau, P.; Baer, S.; Choi, T.; Molitor, F.; Güttinger, J.; Müller, T.; Dröscher, S.; Ensslin, K.; Ihn, T. Coherent electron-phonon coupling in tailored quantum systems. *Nat. Commun.* **2011**, *2*, 239.

(15) Khrapai, V. S.; Ludwig, S.; Kotthaus, J. P.; Tranitz, H. P.; Wegscheider, W. Double-Dot Quantum Ratchet Driven by an Independently Biased Quantum Point Contact. *Phys. Rev. Lett.* **2006**, *97*, 176803.

(16) Hartke, T. R.; Liu, Y.-Y.; Gullans, M. J.; Petta, J. R. Microwave Detection of Electron-Phonon Interactions in a Cavity-Coupled Double Quantum Dot. *Phys. Rev. Lett.* **2018**, *120*, 097701.

(17) Hofmann, A.; Karlewski, C.; Heimes, A.; Reichl, C.; Wegscheider, W.; Schön, G.; Ensslin, K.; Ihn, T.; Maisi, V. F. Phonon spectral density in a GaAs/AlGaAs double quantum dot. *Phys. Rev. Res.* **2020**, *2*, 033230.

(18) Aguado, R.; Kouwenhoven, L. P. Double Quantum Dots as Detectors of High-Frequency Quantum Noise in Mesoscopic Conductors. *Phys. Rev. Lett.* **2000**, *84*, 1986−1989.

(19) Gustavsson, S.; Studer, M.; Leturcq, R.; Ihn, T.; Ensslin, K.; Driscoll, D. C.; Gossard, A. C. Frequency-Selective Single-Photon Detection Using a Double Quantum Dot. *Phys. Rev. Lett.* **2007**, *99*, 206804.

(20) Chen, J. C. H.; Sato, Y.; Kosaka, R.; Hashisaka, M.; Muraki, K.; Fujisawa, T. Enhanced electron-phonon coupling for a semiconductor charge qubit in a surface phonon cavity. *Sci. Rep.* **2015**, *5*, 15176.

(21) Sothmann, B.; Sánchez, R.; Jordan, A. N. Thermoelectric energy harvesting with quantum dots. *Nanotechnology* **2015**, *26*, 032001.

(22) Sánchez, R.; Büttiker, M. Optimal energy quanta to current conversion. *Phys. Rev. B: Condens. Matter Mater. Phys.* **2011**, *83*, 085428.

(23) Thierschmann, H.; Sánchez, R.; Sothmann, B.; Arnold, F.; Heyn, C.; Hansen, W.; Buhmann, H.; Molenkamp, L. W. Three-terminal energy harvester with coupled quantum dots. *Nat. Nanotechnol.* **2015**, *10*, 854.

(24) Jordan, A. N.; Sothmann, B.; Sánchez, R.; Büttiker, M. Powerful and efficient energy harvester with resonant-tunneling quantum dots. *Phys. Rev. B: Condens. Matter Mater. Phys.* **2013**, *87*, 075312.

(25) Jaliel, G.; Puddy, R. K.; Sánchez, R.; Jordan, A. N.; Sothmann, B.; Farrer, I.; Griffiths, J. P.; Ritchie, D. A.; Smith, C. G. Experimental Realization of a Quantum Dot Energy Harvester. *Phys. Rev. Lett.* **2019**, *123*, 117701.

(26) Josefsson, M.; Svilans, A.; Burke, A.; Hoffmann, E.; Fahlvik, S.; Thelander, C.; Leijnse, M.; Linke, H. A quantum-dot heat engine

operating close to the thermodynamic efficiency limits. *Nat. Nanotechnol.* **2018**, *13*, 920−924.
(27) Mazza, F.; Bosisio, R.; Benenti, G.; Giovannetti, V.; Fazio, R.; Taddei, F. Thermoelectric efficiency of three-terminal quantum thermal machines. *New J. Phys.* **2014**, *16*, 085001.
(28) Bergenfeldt, C.; Samuelsson, P.; Sothmann, B.; Flindt, C.; Büttiker, M. Hybrid microwave-cavity heat engine. *Phys. Rev. Lett.* **2014**, *112*, 076803.
(29) Horowitz, J. M.; Gingrich, T. R. Thermodynamic uncertainty relations constrain non-equilibrium fluctuations. *Nat. Phys.* **2020**, *16*, 15−20.
(30) Pietzonka, P.; Seifert, U. Universal Trade-Off between Power, Efficiency, and Constancy in Steady-State Heat Engines. *Phys. Rev. Lett.* **2018**, *120*, 190602.
(31) Verley, G.; Esposito, M.; Willaert, T.; Van den Broeck, C. The unlikely Carnot efficiency. *Nat. Commun.* **2014**, *5*, 4721.
(32) Mahan, G. D.; Sofo, J. O. The best thermoelectric. *Proc. Natl. Acad. Sci. U. S. A.* **1996**, *93*, 7436−7439.
(33) Humphrey, T. E.; Linke, H. Reversible Thermoelectric Nanomaterials. *Phys. Rev. Lett.* **2005**, *94*, 096601.
(34) Entin-Wohlman, O.; Imry, Y.; Aharony, A. Three-terminal thermoelectric transport through a molecular junction. *Phys. Rev. B: Condens. Matter Mater. Phys.* **2010**, *82*, 115314.
(35) Jiang, J.-H.; Entin-Wohlman, O.; Imry, Y. Thermoelectric three-terminal hopping transport through one-dimensional nanosystems. *Phys. Rev. B: Condens. Matter Mater. Phys.* **2012**, *85*, 075412.
(36) Jiang, J.-H.; Entin-Wohlman, O.; Imry, Y. Three-terminal semiconductor junction thermoelectric devices: improving performance. *New J. Phys.* **2013**, *15*, 075021.
(37) Bosisio, R.; Fleury, G.; Pichard, J.-L.; Gorini, C. Nanowire-based thermoelectric ratchet in the hopping regime. *Phys. Rev. B: Condens. Matter Mater. Phys.* **2016**, *93*, 165404.
(38) Jiang, J.-H. Enhancing efficiency and power of quantum-dots resonant tunneling thermoelectrics in three-terminal geometry by cooperative effects. *J. Appl. Phys.* **2014**, *116*, 194303.
(39) Jiang, J.-H.; Kulkarni, M.; Segal, D.; Imry, Y. Phonon thermoelectric transistors and rectifiers. *Phys. Rev. B: Condens. Matter Mater. Phys.* **2015**, *92*, 045309.
(40) Fuhrer, A.; Fröberg, L. E.; Pedersen, J. N.; Larsson, M. W.; Wacker, A.; Pistol, M.-E.; Samuelson, L. Few Electron Double Quantum Dots in InAs/InP Nanowire Heterostructures. *Nano Lett.* **2007**, *7*, 243.
(41) Zannier, V.; Rossi, F.; Ercolani, D.; Sorba, L. Growth dynamics of InAs/InP nanowire heterostructures by Au-assisted chemical beam epitaxy. *Nanotechnology* **2019**, *30*, 094003.
(42) Svilans, A.; Leijnse, M.; Linke, H. Experiments on the thermoelectric properties of quantum dots. *C. R. Phys.* **2016**, *17*, 1096−1108.
(43) Svilans, A.; Burke, A.; Svensson, S.; Leijnse, M.; Linke, H. Nonlinear thermoelectric response due to energy-dependent transport properties of a quantum dot. *Phys. E* **2016**, *82*, 34−38.
(44) Staring, A. A. M.; Molenkamp, L. W.; Alphenaar, B. W.; van Houten, H.; Buyk, O. J. A.; Mabesoone, M. A. A.; Beenakker, C. W. J.; Foxon, C. T. Coulomb-Blockade Oscillations in the Thermopower of a Quantum Dot. *Europhys. Lett.* **1993**, *22*, 57−62.
(45) Dzurak, A. S.; Smith, C. G.; Barnes, C. H. W.; Pepper, M.; Martín-Moreno, L.; Liang, C. T.; Ritchie, D. A.; Jones, G. A. C. Thermoelectric signature of the excitation spectrum of a quantum dot. *Phys. Rev. B: Condens. Matter Mater. Phys.* **1997**, *55*, R10197−R10200.
(46) Scheibner, R.; Novik, E. G.; Borzenko, T.; König, M.; Reuter, D.; Wieck, A. D.; Buhmann, H.; Molenkamp, L. W. Sequential and cotunneling behavior in the temperature-dependent thermopower of few-electron quantum dots. *Phys. Rev. B: Condens. Matter Mater. Phys.* **2007**, *75*, 041301.
(47) Prete, D.; Erdman, P. A.; Demontis, V.; Zannier, V.; Ercolani, D.; Sorba, L.; Beltram, F.; Rossella, F.; Taddei, F.; Roddaro, S. Thermoelectric Conversion at 30 K in InAs/InP Nanowire Quantum Dots. *Nano Lett.* **2019**, *19*, 3033−3039.
(48) Thierschmann, H.; Henke, M.; Knorr, J.; Maier, L.; Heyn, C.; Hansen, W.; Buhmann, H.; Molenkamp, L. W. Diffusion thermopower of a serial double quantum dot. *New J. Phys.* **2013**, *15*, 123010.
(49) Goldozian, B.; Kiršanskas, G.; Damtie, F. A.; Wacker, A. Quantifying the impact of phonon scattering on electrical and thermal transport in quantum dots. *Eur. Phys. J.: Spec. Top.* **2019**, *227*, 1959−1967.
(50) Josefsson, M.; Svilans, A.; Linke, H.; Leijnse, M. Optimal power and efficiency of single quantum dot heat engines: Theory and experiment. *Phys. Rev. B: Condens. Matter Mater. Phys.* **2019**, *99*, 235432.
(51) Blick, R. H.; Pfannkuche, D.; Haug, R. J.; Klitzing, K. v.; Eberl, K. Formation of a Coherent Mode in a Double Quantum Dot. *Phys. Rev. Lett.* **1998**, *80*, 4032−4035.
(52) Oosterkamp, T. H.; Fujisawa, T.; van der Wiel, W. G.; Ishibashi, K.; Hijman, R. V.; Tarucha, S.; Kouwenhoven, L. P. Microwave spectroscopy of a quantum-dot molecule. *Nature* **1998**, *395*, 873−876.
(53) Gustavsson, S.; Studer, M.; Leturcq, R.; Ihn, T.; Ensslin, K.; Driscoll, D. C.; Gossard, A. C. Detecting single-electron tunneling involving virtual processes in real time. *Phys. Rev. B: Condens. Matter Mater. Phys.* **2008**, *78*, 155309.
(54) Kiršanskas, G.; Pedersen, J.; Karlström, O.; Leijnse, M.; Wacker, A. QmeQ 1.0: An open-source Python package for calculations of transport through quantum dot devices. *Comput. Phys. Commun.* **2017**, *221*, 317−342.
(55) Weinmann, D.; Häusler, W.; Kramer, B. Spin Blockades in Linear and Nonlinear Transport through Quantum Dots. *Phys. Rev. Lett.* **1995**, *74*, 984−987.
(56) Ono, K.; Austing, D. G.; Tokura, Y.; Tarucha, S. Current Rectification by Pauli Exclusion in a Weakly Coupled Double Quantum Dot System. *Science* **2002**, *297*, 1313−1317.
(57) Johnson, A. C.; Petta, J. R.; Marcus, C. M.; Hanson, M. P.; Gossard, A. C. Singlet-triplet spin blockade and charge sensing in a few-electron double quantum dot. *Phys. Rev. B: Condens. Matter Mater. Phys.* **2005**, *72*, 165308.
(58) Nadj-Perge, S.; Frolov, S. M.; van Tilburg, J. W. W.; Danon, J.; Nazarov, Y. V.; Algra, R.; Bakkers, E. P. A. M.; Kouwenhoven, L. P. Disentangling the effects of spin-orbit and hyperfine interactions on spin blockade. *Phys. Rev. B: Condens. Matter Mater. Phys.* **2010**, *81*, 201305.
(59) Jiang, J.-H.; Imry, Y. Enhancing Thermoelectric Performance Using Nonlinear Transport Effects. *Phys. Rev. Appl.* **2017**, *7*, 064001.


https://dx.doi.org/10.1021/acs.nanolett.0c04017
*Nano Lett.* 2021, 21, 988−994